MATERIALS CHEMISTRY FRONTIERS

RESEARCH ARTICLE

View Article Online
View Journal | View Issue

Cite this: *Mater. Chem. Front.*, 2025, **9**, 3197

Stabilization of the cubic π-phase of SnS by calcium substitution

Neeraj Mishra, †[ab] Susmita Paul, †[ac] Lonia R. Friedlander, [c] Yuval Golan *[ac] and Guy Makov *[ac]

The cubic phase of tin monosulphide, π-SnS, is of significant interest due to its attractive properties, such as a wider band gap suitable for solar photovoltaic application and being easier to epitaxially deposit onto technologically relevant semiconductors compared to the thermodynamically stable orthorhombic phase of α-SnS. Recently, we reported cation-assisted phase control for obtaining π-SnS rather than α-SnS using Pb^{2+} cations with a concentration of ∼20 cation percent (cat%). However, replacing Pb^{2+} with alternative non-toxic, environmentally friendly cations for cubic phase stabilization would be clearly advantageous. We have computationally investigated the energetics and electronic properties of calcium ion impurities in both SnS polymorphs. We found that addition of Ca^{2+} cations enables phase control of SnS grown from solution from α-SnS to π-SnS. Experimentally, we observed compact films of π-SnS after incorporating Ca^{2+} cations. Computational results indicated that ∼11 cat% of Ca^{2+} ions are required for preferred growth of π-SnS over α-SnS. Furthermore, the presence of an intermediate layer of CaS is computationally predicted to significantly contribute to the stabilization of the π-SnS phase, thereby reducing the Ca concentration required, which aligns well with experimental observations. Subsequently, we find that CaS is a promising substrate for epitaxial growth of π-SnS in the (111) orientation. Moreover, the bandgap of π-SnS decreased slightly with increasing concentration of Ca cations in the material. These results can facilitate the bulk scale synthesis of π-SnS material, bringing it closer to practical utility for a range of applications.

Received 28th May 2025,
Accepted 1st September 2025

DOI: 10.1039/d5qm00399g

rsc.li/frontiers-materials

Introduction

Tin monosulfide (SnS) holds promising characteristics of low toxicity, cost-effectiveness, and earth abundance.[1–4] SnS, a member of the IV–VI semiconductor family, features a narrow band gap and demonstrates optical activity in the near-infrared region.[5] SnS possesses high absorption properties and high hole mobilities, which provides its potential applications in areas of solar cells,[1,3,4,6] field effect transistors,[7] photodetectors,[2,8] gas sensors,[9] and Li-ion and Na-ion batteries.[10]

At room temperature, SnS manifests two primary polymorphs: the ground state orthorhombic phase (α-SnS) and the metastable cubic phase (π-SnS), first reported in 2015.[11,12] The lattice parameters for orthorhombic α-SnS are a = 4.329 Å, b = 11.192 Å, and c = 3.984 Å.[13–15] For π-SnS, the lattice parameter has been reported in the range of 11.595–11.7 Å.[11,16]

Nair *et al.* investigated solar cells featuring absorber layers made from the α-SnS phase, the π-SnS phase, and a mixture of these two phases.[17] Their research revealed that solar cells with absorber layers incorporating both the α- and π-SnS phases exhibited significantly enhanced open-circuit voltage (V_{oc}), conversion efficiency (η), and fill factor (FF) compared to those with layers made from a single-phase.[17]

A variety of techniques have been employed to produce SnS thin films, including vacuum evaporation,[18–20] spray pyrolysis,[21–23] electrodeposition,[24,25] radio frequency (RF) sputtering,[26–28] atomic layer deposition (ALD),[29] and ultrasonication.[30] Among these, chemical solution deposition (CD) stands out as a cost-effective and straight forward method for growing thin films, making it ideal for large-scale industrial applications.[31,32] This technique has been extensively used for different thin film materials,[32–37] including SnS.[38–41] SnS films have been successfully deposited from solution onto multiple substrates, such as glass, silicon (Si), fluorine-doped tin oxide (FTO), and GaAs.[42–45]

Foreign impurities in SnS thin films and nanoparticles have been shown to alter their properties, including electrical, optical, structural, and magnetic characteristics. In particular,

[a] *Department of Materials Engineering, Ben-Gurion University of the Negev, Beer Sheva, 8410501, Israel. E-mail: makovg@bgu.ac.il, ygolan@bgu.ac.il*
[b] *Department of Chemical and Materials Engineering, University of Alberta, Edmonton, AB, T6G 2V4, Canada*
[c] *Ilse Katz Institute for Nanoscale Science and Technology, Ben-Gurion University of the Negev, Beer Sheva, 8410501, Israel*
† These authors contributed equally to this work.

various elements, such as Se,[46] In,[47–49] Ni,[50] Cu,[51] Zn,[52,53] Al,[54] Bi,[55,56] Sb,[57] Ag,[58] Cd,[59] and Fe,[60–62] were used to manipulate the properties of SnS thin films and nanoparticles.

Studies on Pb incorporation in SnS thin films have highlighted their potential for optoelectronic applications due to enhanced photocurrent, carrier concentration, and mobility. Niknia *et al.* found that Pb^{2+} doping in α-SnS increased the grain size and reduced the bandgap, enhancing the photocurrent.[63] Sebastian *et al.* observed that Pb^{2+} doping improved the grain size, carrier concentration, and Hall mobility in SnS thin films.[64]

Furthermore, Chalapathi *et al.* reported that Pb^{2+} doping in the cubic π-SnS phase altered structural, optical, and electrical properties, reducing the bandgap and increasing hole mobility.[65] Additionally, PbS intermediate layers have been shown to be significantly beneficial for the epitaxial growth of π-SnS films on GaAs.[66] Interestingly, a similar trend was observed in MBE-deposited SnSe thin films, where small amounts of Pb were shown to be instrumental for obtaining high-quality growth on GaAs substrates.[67,68] Our recent work further demonstrated that Pb^{2+} promotes the compactness, phase purity, and growth rate of solution-deposited π-SnS thin films. Increased π-SnS content was obtained with increasing Pb^{2+} concentration in solution under conditions shown to otherwise result in pure α-SnS, the thermodynamically stable phase of tin monosulfide.[15] We modelled the Pb impurities in both polymorphs using density functional theory (DFT). The calculated critical concentration of Pb cations to stabilize the π-SnS phase over the stable orthorhombic polymorph was 20 at%, in notable agreement with the experimental results.[15]

The search for alternative cations to stabilize the cubic π-phase of SnS over its orthorhombic polymorph remains important due to the toxic nature of previously used Pb cations. Identifying safer and equally effective cationic alternatives could support broader applications and meet environmental safety standards. Due to the similar oxidation state of Ca^{2+} in CaS and Pb^{2+} in PbS, along with their comparable rocksalt crystal structure and closely matched lattice constants, we hypothesized that Ca^{2+} can serve as an equally suitable cation for stabilizing the π-SnS phase. This hypothesis was proved to be correct both experimentally and computationally. In this work, we have computationally and experimentally explored the effect of calcium cation impurities on the stabilization and physical properties of the cubic π-SnS phase.

Methodology

Computational methods

Modelling of π-SnS and α-SnS was performed to calculate Ca defects using density functional theory (DFT) in the plane-wave pseudopotential approach. All calculations were performed using the first-principles DFT package Quantum ESPRESSO[69] with pseudopotentials obtained from the Garrity, Bennett, Rabe, and Vanderbilt database.[70] The Perdew–Burke–Ernzerhof (PBE) generalized gradient approximation[71] was employed for exchange and correlation energy terms without relativistic corrections. Furthermore, norm-conserving pseudopotentials[72] within GGA-PBE approximation were implemented to investigate the band structure and optical properties. Note that the PBE band gaps are underestimated due to the well-known band-gap error.[73] However, the PBE functional captures the bandgap of SnS in reasonably good agreement with the HSE functional.[74,75] A cutoff energy of 60 Ry in the plane-wave expansion of the wave functions was applied. Ca defects were calculated in $2 \times 2 \times 2$ supercells of α-SnS with 64 atoms; however, unit cells of π-SnS with 64 atoms were considered for defect modelling. The *k*-point sampling employed in calculations for π-SnS and α-SnS was $4 \times 4 \times 4$ and $8 \times 8 \times 4$, respectively, and $16 \times 16 \times 16$ for Sn and Ca metals.

The thermodynamic stability of Ca defects in both phases of SnS can be determined by the calculation of their formation energies. The formation energy of the defects can be calculated as[73]

$$U^{f}[Ca_{Sn}^{q}] = E_{tot}[Ca_{Sn}^{q}] - E_{tot}[\text{bulk}] - n_i\mu_{Ca} + n_i\mu_{Sn} + q(E_{VBM} + \Delta E_F + \Delta V) \quad (1)$$

where $U^{f}[Ca_{Sn}^{q}]$ is the formation energy of the defect Ca_{Sn} with charge q, $E_{tot}[Ca_{Sn}^{q}]$ is the total energy of a supercell containing a defect after the relaxation of the ion positions, $E_{tot}[\text{bulk}]$ is the total energy of a bulk (perfect) supercell with the same number of atoms, n_i is the number of atoms added and removed from the supercell, μ_{Ca} and μ_{Sn} are the chemical potentials of Ca and Sn atoms, respectively, and ΔE_F is the Fermi level referenced to the valence band maximum (VBM) E_{VBM}. The VBM is referenced to the pure cell, and electrostatic potentials between the pristine cell and the defect supercell are aligned by adding a term ΔV. This term, ΔV, is taken as the difference in electrostatic potentials between the atomic site farthest from the defect in the defect supercell and its equivalent site in the defect-free cell.[76] For a neutral defect, q equals zero in eqn (1).

For a material with a diatomic basis, the chemical potential involved in defect formation energy calculations generally has an arbitrary degree of freedom, controlled by experimental boundary conditions. Formation energies per atom of π-SnS and α-SnS were calculated and found to be nearly the same (the difference is 5×10^{-3} eV) and in accord with the previous studies.[15,16,77,78] Therefore, the chemical potential range of Sn and S should be the same in both phases. To maintain stable π-SnS and α-SnS compounds, the chemical potentials of Sn and S must satisfy equation:

$$\mu_{Sn} + \mu_S = \Delta H^{f}(SnS^{\pi/\alpha}) + \mu_{Sn}^{bulk} + \mu_S^{bulk} \quad (2)$$

or equivalently,

$$\Delta\mu_{Sn} + \Delta\mu_S = \Delta H^{f}(SnS^{\pi/\alpha}) \quad (3)$$

where $\Delta H^{f}(SnS^{\pi/\alpha})$ is the heat of formation of π-SnS and α-SnS.

However, to put reasonable limits on the chemical potentials of the Ca substitution defects, we consider restrictions that prevent not only the precipitation of the bulk phases of the

dopant but also prevent the formation of phases of the dopant and the host atoms.

$$\Delta\mu_{Ca} + \Delta\mu_{S} \leq \Delta H^{f}(CaS) \quad (4)$$

Moreover, the surface and interface energies were obtained using eqn (5) and (6). The surface energy π-SnS is obtained from:

$$\sigma_{\pi\text{-SnS}} = \frac{\left(E^{tot}_{Slab(\pi\text{-SnS})} - E^{bulk}_{(\pi\text{-SnS})}\right)}{2A} \quad (5)$$

and the interfacial energy:

$$\sigma_{\pi\text{-SnS/CaS}} = \frac{\left(E^{tot}_{Slab(\pi\text{-Sn/CaS})} - E^{bulk}_{\pi\text{-SnS}} - E^{bulk}_{CaS}\right)}{2A} \quad (6)$$

where $E^{tot}_{slab(\pi\text{-SnS})}$ is the total energy of slab π-SnS, $E^{bulk}_{(\pi\text{-SnS})}$ is the total energy of the bulk of the π-SnS system having the same number of atoms, $E^{tot}_{slab(\pi\text{-SnS/CaS})}$ is the total energy of the heterostructure system, and A is the surface area of the slab.

Experimental methods

Materials. $CaCl_2$ (97%, Aldrich), $SnCl_2{\cdot}2H_2O$ (≥99.99%, Sigma-Aldrich), $Ca(CH_3COO)_2{\cdot}H_2O$ (≥99.0%, Sigma-Aldrich), triethanolamine (TEA) (≥99.0%, Sigma-Aldrich), and thioacetamide (≥99.0%, Sigma-Aldrich) were used without further purification. Ammonium hydroxide (25% w/w), acetic acid (Bio-Lab, analytical grade), acetone (Bio-Lab, technical grade), and 2-propanol (Bio-Lab, 99.8%) were used without further purification. Distilled water (DIW) was obtained using a Millipore Direct Q3 water purification system. Monocrystalline GaAs (100) wafers (undoped, epi-polished with _0.11 miscut) were manufactured by AXT Inc and purchased from Geo Semiconductor (UK) Ltd. Fluorine-doped tin oxide (FTO) substrates were purchased from XOP GLASS (TEC 15, sheet resistance 12–14 Ohm cm^2).

Substrate preparation. Double-side polished GaAs(100) wafers were cleaved into 1.5 × 2 cm^2 pieces and sonicated in aqueous detergent solution for 10 min at room temperature. The wafers were then washed with DIW, acetone, and 2-propanol in that order. Finally, the substrates were dried under a N_2 flow. The FTO substrates were treated similarly.

Deposition procedure. (a) Surface pretreatment: surface pretreatment was carried out based on our previous experience with Pb^{2+} cations where treatment in Pb^{2+} solution was shown to activate the substrate surface.[15,44] In the present study, 0.35 M calcium chloride solution was prepared in a 50 ml beaker and degassed under N_2 purging for one hour. The beaker was then placed in a thermostatic bath at 50 °C and the substrates were immersed in the solution for one day, then the substrates were rinsed with water and immediately placed into the deposition bath. This pretreatment of the substrates in the calcium chloride solution resulted in adsorption of Ca^{2+} cations on the GaAs substrates, as shown in Fig. S1, SI.

(b) Thin film preparation: for the deposition of the SnS thin film, the aqueous solution was prepared containing 0.04 M $SnCl_2{\cdot}2H_2O$, 0.5 M acetic acid, 1.1 M TEA, and 0.4 M ammonium hydroxide with a final volume of 50 ml. The TEA and ammonium hydroxide serve as complexing agents, binding to the metal cations and preventing them from quickly reacting or precipitating out of the solution. For introducing Ca^{2+}, different amounts of $Ca(CH_3COO)_2{\cdot}H_2O$ were added in the solution. The substrates were immersed in the deposition solution immediately after adding thioacetamide to reach a final concentration of 0.08 M. Depositions were carried out at 40 °C for 3 hours.

Characterization. Grazing incidence X-ray diffraction (GIXD) measurements were performed on thin films of the samples using a Malvern Panalytical Empyrean III diffractometer equipped with a position sensitive PIXcel3D detector and iCore/dCore automated optics combination. Cu Kα radiation (λ = 1.5405 Å) was used as the incident radiation, with a fixed incident beam angle of 0.5°. Two GIXD scans were performed: a standard scan with a step size of 2θ = 0.10° was collected for all samples over a 2θ range of 20–50° with three sequential measurements collected and summed to produce the final GIXD diffractogram. A high-resolution GIXD follow-up scan was also performed on select samples in the 2θ range of 20–37.5°, with a step size of 0.08° and six sequential measurements collected and summed. High resolution scanning electron microscopy (HRSEM) was carried out using an FEI Verios 460L HRSEM. Topography images were taken using 3 keV to 5 keV acceleration voltages and beam currents of 25 pA to 50 pA. The measurements were carried out without coating the samples. Transmission electron microscopy (TEM) was performed using a JEOL JEM-2100F operating at an accelerating voltage of 200 kV. EDS analysis was carried out in the TEM using an Oxford Instruments X-Max 65T SDD detector. AZtec software (v. 3.3) was used for EDS data analysis. X-ray photoelectron spectroscopy (XPS) measurements were carried out using an ESCALAB 250 spectrometer with a monochromatic Al X-ray source (excitation energy 1486.6 eV) at a base pressure of 1 × 10^{-9} mbar. Raman spectroscopy was carried out on a LabRAM HR Evolution (HORIBA, France) micro-Raman system equipped with cold stage and a rotating polarizer. The excitation source was a 532 nm HeNe laser with a power of 3 mW on the sample. Optical absorption measurements were performed in the range 400–1000 nm using a Cary 5000 UV-vis-NIR spectrophotometer equipped with a PbSmart detector. Samples for inductively coupled plasma optical emission spectrometry (ICP-OES) were prepared by initially cleaning the backside of the FTO substrates with dilute acid, and then dissolving the SnS films in an aqueous solution of 70% HNO_3. The resulting solutions were analyzed using a SPECTRO ARCOS ICP-OES spectrometer manufactured by Spectro Ametek.

Results and discussion

The optimized lattice constants and bandgap for cubic π-SnS and orthorhombic α-SnS were calculated (see Table 1) and found to be a = 11.885 Å and a = 4.023 Å, b = 4.441 Å, c = 11.429 Å, in accord with reported experimental values

Table 1 Lattice constants (Å) and band gap (eV) calculated for π-SnS and α-SnS

Lattice constant (Å)			
SnS phase	Our calculation	Previous calculation[8]	Experimental value[7]
π-SnS	a = 11.885	a = 11.885	a = 11.594
α-SnS	a = 4.023	a = 4.03	a = 3.987
	b = 4.441	b = 4.42	b = 4.334
	c = 11.429	c = 11.41	c = 11.20
Band gap (eV)			
π-SnS	1.34	1.34[9]	1.53[10]
α-SnS	1.04	1.06[9]	1.25[10]

a = 11.594 Å, and a = 3.987 Å, b = 4.334 Å, and c = 11.20 Å,[79] and other theoretical studies reported a = 11.885 Å, and a = 4.03 Å, b = 4.42 Å, and c = 11.41 Å.[80] Moreover, an indirect bandgap was obtained for cubic π-SnS and orthorhombic α-SnS, *i.e.*, 1.31 eV and 1.04 eV, respectively, in good agreement with a previous theoretical result of 1.34 eV[81] and 1.06 eV,[81] respectively, slightly underestimating the reported experimental results of 1.53 eV[82] and 1.25 eV,[82] as might be expected.

The crystal structures of π-SnS and α-SnS are illustrated in Fig. 1. The low-symmetry π-SnS unit cell with 64 atoms is depicted in Fig. 1 and compared with a 2 × 2 × 2 supercell of α-SnS, which contains 8 atoms in each unit cell, altogether 64 atoms in the supercell. The substitutional sites in π-SnS and α-SnS are highlighted in red in Fig. 1.

The thermodynamic stability of Ca incorporation at selected concentrations was examined in both phase systems by calculating the formation energy using eqn (1). From energetic calculations, the difference in the formation enthalpy of α-SnS and π-SnS is very small, 5 × 10^{-3} eV $atom^{-1}$. Therefore, the chemical potential of the components (Sn and S) in both systems can be considered equal. Hence, doping with suitable elements at sufficient concentrations may cause π-SnS to be preferred over the ground state α-SnS phase. Given the structural similarity between PbS and CaS, we hypothesized that the Ca^{2+} cation may serve a role similar to that of Pb^{2+} cations in SnS systems. Incorporating Ca^{2+} cations could thermodynamically stabilize the π-SnS phase in comparison to the ground state α-SnS phase. To test this hypothesis, we recalculated the formation enthalpy of both systems for selected concentrations of calcium cations.

The defect formation energies of Ca incorporated at Sn substitutional sites (using the conventional chemical potential

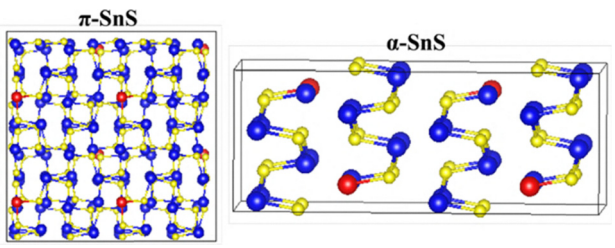

Fig. 1 Schematic representation of π-SnS and α-SnS with four Ca substitutions at the Sn sites in both supercell models.

Table 2 The formation energies (U) of Ca substitution in π-SnS and α-SnS, the difference of the formation energy (ΔU) between π-SnS and α-SnS, the difference of formation energy per atom (ΔE), difference in total enthalpy per atom (ΔH) and equilibrium concentrations (c) of Ca for selected fixed concentrations

	$U^f[Ca_{Sn}]$ (eV)					
c_{fix}	π-SnS	α-SnS	$\Delta U^f[Ca_{Sn}]$ (meV)	$\Delta E^f[Ca_{Sn}]$ (meV $atom^{-1}$)	$\Delta H^f_{\pi\text{-SnS}/\alpha\text{-SnS}}[Ca_{Sn}]$ (meV $atom^{-1}$)	c (cat%)
0	N/A	N/A	N/A	N/A	5	N/A
3.13	−1.86	−1.77	−90	−1.4	3.6	11.2 ± 1
12.5	−7.87	−7.52	−350	−5.5	−0.5	11.4 ± 3.5

of Ca from the FCC elemental phase) were calculated for α-SnS and π-SnS (Table 2). We found negative defect formation energies of Ca substitution in both systems, with a difference of 0.09 eV in favour of the π-SnS phase. Comparing this result with the previous study for Pb, the energy difference obtained was thrice as high for Ca incorporation (in favour of π-SnS),[15] which results in Ca being a more suitable cation for stabilizing π-SnS, requiring relatively lower substitutional concentration.

For Ca_{Sn} substitutions to facilitate the transformation of the stable SnS phase from α-SnS to π-SnS, the formation enthalpy of π-SnS ($\Delta H^f_{\pi\text{-SnS}}[Ca_{Sn}]$) should be lower than that of α-SnS ($\Delta H^f_{\alpha\text{-SnS}}[Ca_{Sn}]$), *i.e.*, $\Delta H^f_{\pi\text{-SnS}}[Ca_{Sn}] < \Delta H^f_{\alpha\text{-SnS}}[Ca_{Sn}]$.

We calculated the defect formation energies of Ca for selected concentrations. Ca substitution in π-SnS was found to be more energetically favorable than in α-SnS, with energy gains of 0.09 eV and 0.35 eV for 3.13 cat% and 12.5 cat% substituted Ca atoms in the simulated supercell, respectively.

We determined the equilibrium Ca defect concentration, c, at which the π-SnS phase becomes more stable than the α-SnS phase. Assuming a linear relationship between defect concentration and formation energy, the relative formation energy of the SnS phases with Ca substitutional defects is expressed by eqn (7).

$$\Delta H^f_{\pi\text{-SnS}/\alpha\text{-SnS}}[Ca_{Sn}] = \Delta H^f_{\pi\text{-SnS}/\alpha\text{-SnS}} + c'\Delta E^f[Ca_{Sn}] \quad (7)$$

$$c = c' \times c_{fix} \quad (8)$$

where $\Delta H^f_{\pi\text{-SnS}/\alpha\text{-SnS}}[Ca_{Sn}]$ represents the difference in lattice formation energies per atom between π-SnS and α-SnS containing Ca defects at concentration c. $\Delta H^f_{\pi\text{-SnS}/\alpha\text{-SnS}}$ denotes the formation energy difference per atom between pure π-SnS and α-SnS, while $\Delta E^f[Ca_{Sn}]$ corresponds to the difference in formation energies per atom of π-SnS and α-SnS with concentration c_{fix} of Ca.

Setting the left-hand side of eqn (7) to zero allows us to estimate the desired concentration, c. The calculated enthalpy differences and c' (calculated using eqn (8)) for selected values of c_{fix} are reported in Table 2. We calculated critical concentration, c, for c_{fix} of 3.13 cation percent (cat%, namely the percentage of Ca cations out of the total number of cations) Ca substitution to be 11.2 at% (complete calculations can be found in the SI). The difference in the lattice formation energy ($\Delta H^f_{\pi\text{-SnS}/\alpha\text{-SnS}}[Ca_{Sn}]$) of both phases was found to decrease to 4.65 meV $atom^{-1}$, favoring α-SnS. For a fixed Ca concentration

of 12.5 cat%, the difference in lattice formation energy nearly vanished, with a value of 0.4 meV atom^{-1}—below the computational error limit. We used these data to calculate the critical equilibrium concentration value c using eqn (7) and found it to be 11.4 cat%.

For 25 cat% substitution of Ca, the total energy of π-SnS was found to be lower than that of α-SnS and became the ground state phase of SnS as expected (Table 2). Furthermore, we determined the optimized lattice constants for 25 cat% Ca (equivalent to eight Ca substitutions) in both π-SnS and α-SnS. Our results show that the lattice constants remain almost unchanged compared to the pristine material, with a difference of approximately 1% for π-SnS.

Finally, we calculated the bandgap of the bulk and Ca-substituted systems, and their values are reported in Table 3. The bandgap of π-SnS was found to decrease slightly with increasing Ca substitution concentrations in the system (Table 3), as confirmed by the experimental measurements reported below. The calculated bandgap values underestimate the experimental results (Fig. 4), which is a known limitation of the PBE-GGA approximation (Table 1).

Based on these computational findings, we moved to experimentally study the effect of Ca^{2+} incorporation on the phase stability of SnS thin films synthesized by CD.[44] The amount of $Ca(CH_3COO)_2{\cdot}H_2O$ (Ca/Sn molar ratio ranges from 0.02 to 0.14) was changed to vary the concentrations of Ca^{2+} in the reaction solution. HRSEM of the pristine SnS thin film exhibits vertically stacked platelet morphology (Fig. 2a). Fig. 2b–d represent the gradual changes in morphology of the deposited SnS films upon addition of Ca^{2+} cations to the deposition bath. The morphology remains unchanged up to 6% Ca^{2+} (mole percentage; Fig. 2b), however at higher concentrations of Ca^{2+}, a clear change in film morphology is observed. At 10% Ca^{2+} cation concentrations, rounded grains along with the vertical platelets start to appear (Fig. 2c). At 12% Ca^{2+} concentrations, the film morphology is exclusively composed of rounded grains (Fig. 2d). At 14% Ca^{2+} cation concentrations, HRSEM indicated the formation of large box shaped particles underneath the film (Fig. S2a, SI). Cross-sectional TEM analysis was carried out to understand the nature of the large box shape particles. TEM images indicate the formation of a distinct layer inner to the SnS layer (Fig. S2b, SI). Analyzing the composition of the layer using EDS in TEM indicated that the atomic concentration ratio in the additional layer is Ca : Sn : O = 20 : 15 : 65. However, we could not obtain any SAED pattern from the layer, which pointed out to the amorphous/very weak crystalline nature of the layer (Fig. S2c, SI). The vertically stacked platelets and the rounded grains are typical, characteristic morphologies of the α-SnS and π-SnS thin film, respectively.[15,44] Hence, HRSEM suggested the formation of a different phase obtained upon incorporation of increasing concentrations of Ca^{2+}cations.

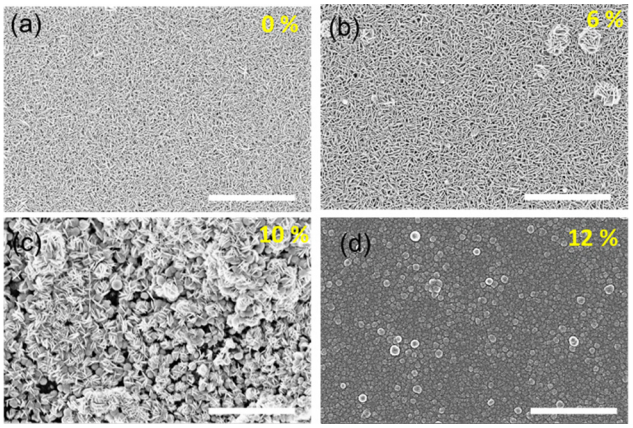

Fig. 2 HRSEM images of SnS thin films deposited onto GaAs(100) substrates from solutions containing (a) 0% Ca^{2+}, (b) 6% Ca^{2+}, (c) 10% Ca^{2+}, and (d) 12% Ca^{2+}. All scale bars correspond to 3 μm.

To verify the phase composition upon Ca^{2+} addition, GIXD measurements were performed (Fig. 3). The GIXD pattern of the film with 0% Ca^{2+} (black curve, Fig. 3a) exhibits a single peak corresponding to the (111) plane of the orthorhombic crystallographic phase (α-phase) (COD file #1011253; space group: *Pmcn* (62)). The GIXD pattern of the film with 6% Ca^{2+} exhibits somewhat improved crystallinity, however it still exhibits the pure α-phase (red curve, Fig. 3a), which is consistent with the HRSEM images. Upon increasing the Ca^{2+} concentration to 10%, a new peak appears at 2θ = 26.7°, corresponding to the (222) plane of the cubic π-phase of SnS (ICDD # 04-023-2702; space group: $P2_13$ (198)). The GIXD pattern of the film with 10% Ca^{2+} also exhibits a broad peak in the 2θ range of 30.7–31.9° (blue curve, Fig. 3a). From the high-resolution measurement in the small 2θ range (20°–36°) (Fig. 3b), we can distinguish the peak corresponding to the (400) plane of the π-phase, which nearly overlaps with that corresponding to the (111) plane of the α-phase, contributing together to the originally observed broad peak. At 12% Ca^{2+} concentration, only peaks corresponding to the π-phase exist (green curve, Fig. 3a).[44] The observed changes in the XRD patterns of the films deposited in the presence of different concentrations of Ca^{2+} cations confirm the stabilization of the π-phase over the α-phase and are consistent with the HRSEM results.

Raman spectroscopy was employed to further investigate the SnS films deposited with various concentrations of Ca^{2+} cations. The Raman spectra (Fig. 4a) of the SnS film with 0% Ca^{2+} exhibit peaks at 93 cm^{-1}, 160 cm^{-1}, and 227.6 cm^{-1} corresponding to the A_g and B_{3g} modes of the α-SnS.[44] In the case of 6% Ca^{2+}, the Raman spectrum (Fig. 4a) exhibits similar peaks corresponding to the A_g and B_{3g} modes of α-SnS. At 10% Ca^{2+} concentrations, new peaks at 193 cm^{-1} and 224 cm^{-1} corresponding to the A_g mode of π-SnS[11] appeared along with the peak at 93 cm^{-1} of α-SnS (Fig. 4a). The Raman spectrum of

Table 3 Bandgap (eV) of π-SnS with Ca substitution for selected fixed concentrations (cat%)

Ca substitution (cat%)	Bandgap (eV)
0	1.34
3.13	1.33
12.5	1.22
25	1.05

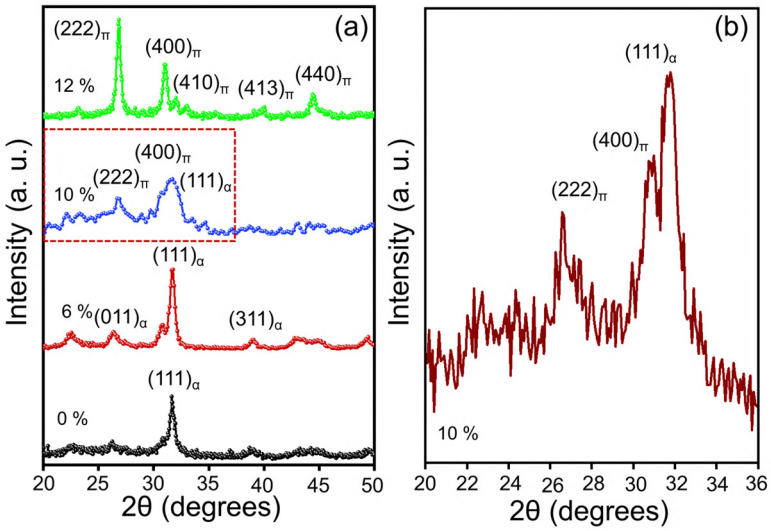

Fig. 3 (a) GIXD pattern of SnS thin films deposited onto GaAs (100) substrates in the presence of 0% Ca^{2+} (black curve), 6% Ca^{2+} (red curve), 10% Ca^{2+}(blue curve), and 12% Ca^{2+} (green curve). (b) GIXD pattern of the SnS thin film deposited with 10% Ca^{2+} over the 2θ range of 20–36°.

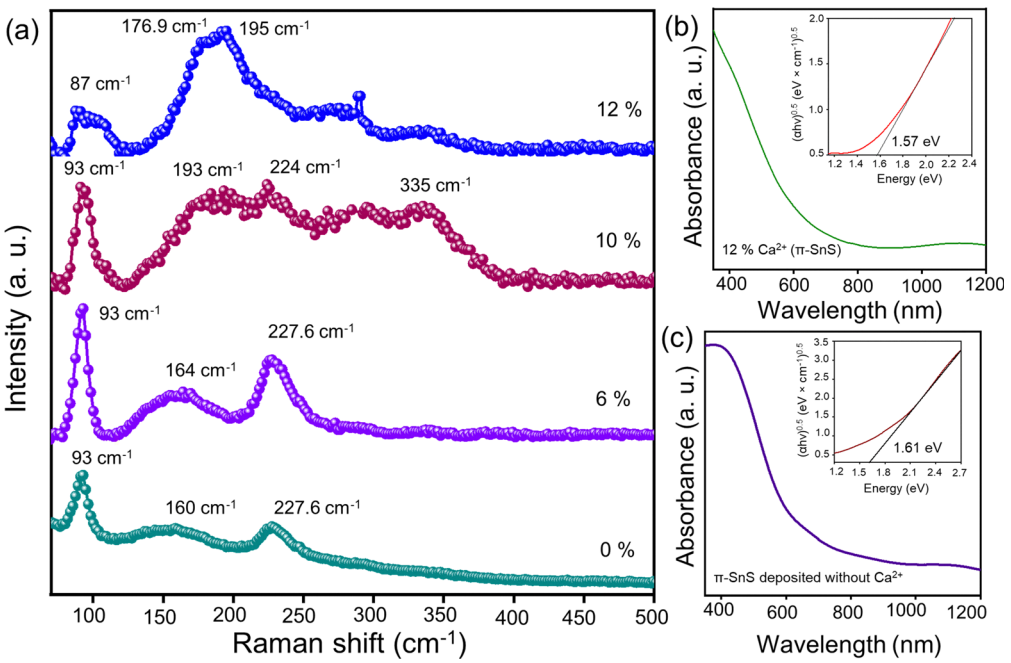

Fig. 4 (a) Raman spectra of SnS films deposited onto GaAs(100) substrates in the presence of 0% Ca^{2+} (cyan curve), 6% Ca^{2+} (violet curve), 10% Ca^{2+} (maroon curve), and 12% Ca^{2+} (blue curve). (b) UV-vis absorption spectra of the SnS film with 12% Ca^{2+} (π-SnS) on FTO coated glass substrates. Inset: Tauc plot indicates an indirect band gap of 1.57 eV for the SnS film deposited with 12% Ca^{2+} which matches with the reported value of π-SnS. (c) UV-vis absorption spectra of the SnS film deposited from the solution following the protocol which generally results in the formation of π-SnS. Inset: Tauc plot indicates an indirect band gap of 1.61 eV demonstrating a slight decrease in the bandgap as a result of Ca-incorporation in π-SnS.

the film with 12% Ca^{2+} concentration exhibits peaks at 87 cm^{-1}, 176.9 cm^{-1}, and 195 cm^{-1}, corresponding to the B_{1g}, B_{3g}, and A_g modes of π-SnS (Fig. 4a).[11] The peak positions obtained are in good agreement with previous Raman measurements for α-SnS and π-SnS, respectively.[11] The Raman spectroscopy results reaffirmed the HRSEM and GIXD results in Fig. 2 and 3, respectively.

Subsequently, we investigated the optical properties of the films deposited with different Ca^{2+} concentrations in solution using UV-vis absorption spectroscopy (Fig. S3, SI). Fig. 4b shows the UV-vis absorption spectra of π-SnS films deposited from a solution containing 12% Ca^{2+} onto FTO coated glass substrates. Tauc plot analysis shows an indirect band gap of 1.57 eV for the film deposited in the presence of 12% Ca^{2+} (inset of Fig. 4b),

Table 4 Surface and interfacial energies (meV Å^{-2}) for π-SnS and CaS systems

Surface/interface	Surface/interface energy (meV Å^{-2})	Previous results (meV Å^{-2})
π-SnS(111) (S-termination)	32.5	32.5,[66] 32.4[78]
CaS(111) (Ca-termination)	49.5	—
π-SnS(111)/CaS(111)	26.1	—

which is in good agreement with the literature values previously reported for π-SnS.[11,15,83] For comparison, we have also measured the absorbance spectra of the π-SnS film deposited following a deposition protocol that generally produces a π-phase SnS film (Fig. 4c). Corresponding Tauc plot analysis shows an indirect band gap of 1.61 eV for the π-SnS film. In summary, this value points out to a slight decrease in the bandgap of π-SnS upon Ca^{2+} incorporation.

XPS measurements were carried out to quantitatively evaluate the amount of Ca^{2+} incorporated into the SnS films. For Ca^{2+} concentrations lower than 10% Ca^{2+} in the bath, we are unable to quantify the presence of Ca^{2+} in the film. However, atomic % calculation from the XPS measurements of the SnS film, deposited with 12% of Ca^{2+}, clearly points to the presence of Ca^{2+} in the SnS film with a Ca to Sn ratio of ~0.02 : 1 (2 cat%). The result is in qualitative agreement with the theoretical calculation, although they differ quantitatively as the data in Table 2 predict a higher critical concentration of Ca^{2+} ions of 11 cat%. The pre-treatment of the substrate with Ca^{2+} cations, followed by subsequent reaction with sulfide in the reaction bath is likely to result in the formation of an ultrathin cubic (rocksalt) CaS intermediate layer which is lattice-matched with the GaAs substrate (less than 1% mismatch) and is likely to strongly stabilize the surface of the incipient π-SnS, yet this could not be verified experimentally, probably due to the ultrathin nature and/or poor crystallinity of the intermediate layer. Computational studies clearly support the above assumption. We modelled the epitaxial growth of a π-SnS(111) overlayer on rocksalt CaS(111) substrate (Fig. 6). The interfacial energy of the π-SnS(111)/CaS(111) heterostructure and the surface energies of π-SnS(111) and CaS(111) were calculated using eqn (5) and (6). The results are given in Table 4. Our calculation reveals that the interfacial energy of the π-SnS(111)/CaS(111) interface is lower than the surface energies of both π-SnS(111) and CaS(111), indicating thermodynamic preference for interface formation over surface exposure. The gain in energy from the difference in interfacial and surface energies is approximately 6.4 meV Å^{-2}, which corresponds to 104 meV per surface atom. This energy gain is sufficient to stabilize the π-SnS phase without incorporation of significant Ca in the bulk. However, experimentally we found that surface treatment is not solely sufficient for stabilizing the π-phase. Nevertheless, Ca substitution is energetically favorable, which suggests that limited incorporation of Ca atoms can occur within the bulk of π-SnS. The survey spectrum of the SnS film deposited with 12 cat% of Ca^{2+} is shown in Fig. S4a, SI. The high-resolution Sn 3d XPS spectrum reveals peaks at 486.4 eV and 494.8 eV, which suggest that there is surface Sn bonding with O (Fig. S4b, SI).[15] The mild surface oxidation of the SnS film is typical for solution-deposited thin films.[15] We have therefore removed the surface oxide layer from the SnS sample by mild etching using Ar ions. After etching, the Sn 3d core-level spectra display peaks at 493.9 eV and 485.5 eV corresponding to the Sn $3d_{3/2}$ and Sn $3d_{5/2}$, respectively (Fig. 5a). The doublet nature of both components is the result of Ar ion

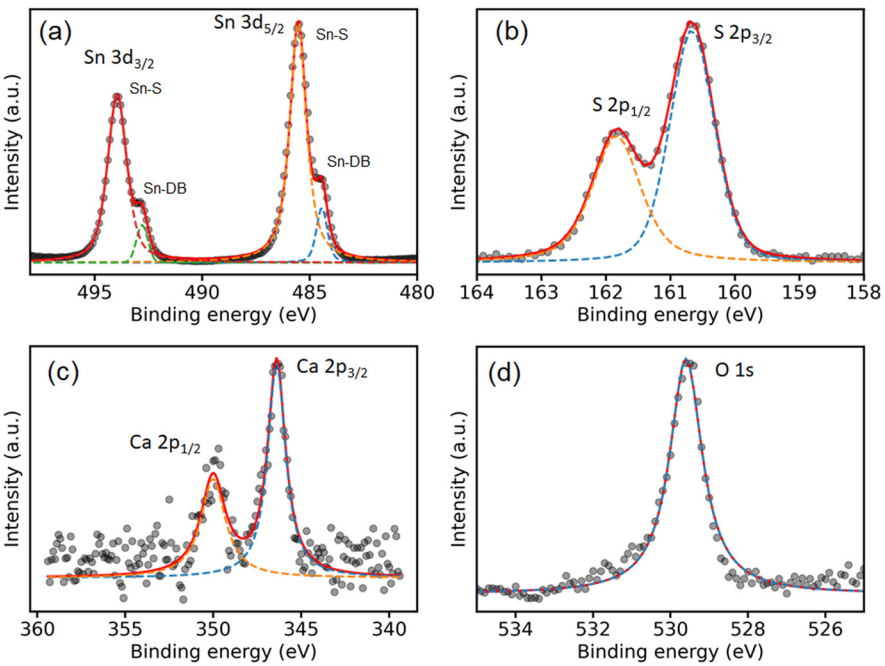

Fig. 5 XPS core-level spectra obtained from an SnS film deposited from a solution with 12 cat% Ca^{2+}, showing (a) Sn 3d (b) S 2p (c) Ca 2p and (d) O 1s.

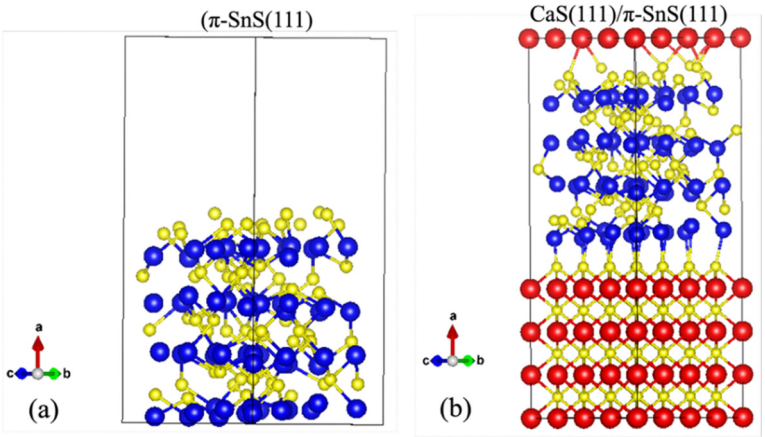

Fig. 6 Structural models used to calculate surface energies: (a) π-SnS(100) slab and (b) interfacial energy CaS(111)/π-SnS(111). The blue, red and yellow atoms represent tin, calcium and sulfur atoms, respectively. Heterostructure CaS(111)/π-SnS(111) is constructed with both anion (sulfur) and cation (Ca or Sn) termination surfaces of CaS(111) and π-SnS(111).

bombardment which leads to the formation of reduced states due to partial destruction of bonds.[15,84] The peaks corresponding to the Sn dangling bonds appear at 492.8 eV and 484.5 eV (Fig. 5a). S 2p core-level spectra reflect peaks at 161.8 eV and 160.7 eV corresponding to S $2p_{1/2}$ and S $2p_{3/2}$, respectively (Fig. 5b). Ca 2p core-level spectra show peaks at 349.9 eV and 346.3 eV corresponding to the Ca $2p_{1/2}$ and Ca $2p_{3/2}$, respectively (Fig. 5c). O 1s core-level spectra show a peak at 529.5 eV (Fig. 5d).

To confirm the amount of Ca incorporated in the film, we performed ICP-OES after dissolving the films in 70% nitric acid. The relative concentrations of the Ca incorporated in the films deposited using 0–12% Ca^{2+} in the solutions are provided in Table S1, SI. The ICP-OES results indicated that the Ca^{2+} concentration in the film deposited with 12% Ca^{2+} in the solution was 3.92% (slightly higher than the concentration of one substitutional atom which is 3.125% or 1/32), in reasonable agreement with the concentration obtained from XPS.

Stabilization of the π-SnS phase with the assistance of Ca^{2+} offers notable advantages over the previously studied Pb^{2+} cations.[15] Pb substitution, while effective, is environmentally undesirable and requires a relatively high concentration (*ca.* ∼20 cat%) to stabilize the π-SnS phase. In comparison, Ca^{2+} offers environmental sustainability and is more effective, theoretically requiring ∼11 cat% to stabilize the π-SnS phase. Notably, similar to PbS substrates, CaS can also serve as a potential substrate for the epitaxial growth of π-SnS overlayers.[66] This is likely to explain the relatively low experimentally measured concentration of approximately 3.92 cat% Ca in the π-SnS phase because surface stabilization is likely to be taking place in addition to bulk stabilization.

Conclusions

The cubic polymorph π-SnS was stabilized with the assistance of non-toxic Ca^{2+} cations. The free enthalpy of Ca incorporation in both SnS phases was calculated using DFT. The defect formation energies for Ca substitution indicate that its incorporation is energetically stable and relatively more favorable in π-SnS. We calculated the critical concentration of Ca substitution, which can lead to the phase stabilization of SnS from α-SnS to π-SnS and found it to be ∼11 cat%. We demonstrated the theoretical prediction of phase stabilization using CD methods and found that Ca^{2+}-cation incorporation can lead to stabilization of π-SnS over α-SnS. Experimental characterization using HRSEM, GIXD, and Raman spectroscopy confirmed the computational results. Interestingly, concentrations of 3.92 cat% Ca^{2+} appear to be sufficient for stabilizing the π-SnS phase and favoring it over the thermodynamically preferred α-SnS. It is likely that the effect of adsorbed Ca onto the substrate can also contribute to the stabilization of π-SnS, decreasing the need for Ca in the bulk by means of substitutional incorporation. The small concentrations of Ca^{2+} in the films did not significantly alter the optical properties of π-SnS.

Author contributions

Dr Neeraj Mishra (computational studies) and Dr Susmita Paul (experimental studies) contributed equally. The manuscript was written through contributions of all authors. All authors have given approval to the final version of the manuscript.

Conflicts of interest

There are no conflicts to declare.

Data availability

The data supporting this article have been included as part of the SI. See DOI: https://doi.org/10.1039/d5qm00399g.

Raw data are available from the repository of the Ilse Katz Institute for Nanoscale Science and Technology at BGU.

Acknowledgements

This work was funded by the Israel Science Foundation, Grant no. 512/23. We thank Dr Lee Shelly (XPS), Dr Mariela Pavan (Raman spectroscopy), Dr Nitzan Maman (FIB-HRSEM), Dr Bar Elisha (ICP-OES) and Dr Vladimir Ezersky (TEM) for expert assistance. S. P. extends sincere appreciation to Dr Noy Zakay for her invaluable assistance.

References

1 R. Banai, M. Horn and J. Brownson, A review of tin(II) monosulfide and its potential as a photovoltaic absorber, *Sol. Energy Mater. Sol. Cells*, 2016, **150**, 112–129.
2 B. Zhou, S. Li, W. Li, J. Li, X. Zhang, S. Lin, Z. Chen and Y. Pei, Thermoelectric properties of SnS with Na-doping, *ACS Appl. Mater. Interfaces*, 2017, **9**, 34033–34041.
3 J. A. Andrade-Arvizu, M. Courel-Piedrahita and O. Vigil-Galán, SnS-based thin film solar cells: perspectives over the last 25 years, *J. Mater. Sci.: Mater. Electron.*, 2015, **26**, 4541–4556.
4 K. R. Reddy, N. K. Reddy and R. Miles, Photovoltaic properties of SnS based solar cells, *Sol. Energy Mater. Sol. Cells*, 2006, **90**, 3041–3046.
5 G. A. Tritsaris, B. D. Malone and E. Kaxiras, Optoelectronic properties of single-layer, double-layer, and bulk tin sulfide: A theoretical study, *J. Appl. Phys.*, 2013, **113**, 233507.
6 R. W. Miles, O. E. Ogah, G. Zoppi and I. Forbes, Thermally evaporated thin films of SnS for application in solar cell devices, *Thin Solid Films*, 2009, **517**, 4702–4705.
7 D. Mudusu, K. R. Nandanapalli, S. R. Dugasani, R. Karuppannan, G. K. R. Reddy, R. G. E. Subramanian and S. H. Park, Metal–insulator–semiconductor field-effect transistors (MISFETs) using p-type SnS and nanometer-thick Al_2S_3 layers, *RSC Adv.*, 2017, **7**, 11111–11117.
8 T. S. Reddy and M. C. S. Kumar, Co-evaporated SnS thin films for visible light photodetector applications, *RSC Adv.*, 2016, **6**, 95680–95692.
9 Y. Qin, Y. Liang, C. Zhou and Y. Bai, Homogeneous heterophase junction based on cubic/orthomorphic SnS for chemiresistive room temperature trace-ethanol sensor, *Sens. Actuators, B*, 2024, **404**, 135285.
10 Z. Wei, L. Wang, M. Zhuo, W. Ni, H. Wang and J. Ma, Layered tin sulfide and selenide anode materials for Li-and Na-ion batteries, *J. Mater. Chem. A*, 2018, **6**, 12185–12214.
11 R. E. Abutbul, E. Segev, L. Zeiri, V. Ezersky, G. Makov and Y. Golan, Synthesis and properties of nanocrystalline π-SnS–a new cubic phase of tin sulphide, *RSC Adv.*, 2016, **6**, 5848–5855.
12 A. Rabkin, S. Samuha, R. E. Abutbul, V. Ezersky, L. Meshi and Y. Golan, New nanocrystalline materials: a previously unknown simple cubic phase in the SnS binary system, *Nano Lett.*, 2015, **15**, 2174–2179.
13 I. Pallikara and J. M. Skelton, Phase stability of the tin monochalcogenides SnS and SnSe: a quasi-harmonic latticedynamics study, *Phys. Chem. Chem. Phys.*, 2021, **23**, 19219–19236.
14 R. E. Abutbul, E. Segev, S. Samuha, L. Zeiri, V. Ezersky, G. Makov and Y. Golan, A new nanocrystalline binary phase: synthesis and properties of cubic Tin monoselenide, *CrystEngComm*, 2016, **18**, 1918–1923.
15 N. Zakay, N. Mishra, N. Maman, A. Rashkovskiy, A. Schlesinger, R. E. Abutbul, V. Ezersky, D. Azulay, G. Makov and Y. Golan, Phase control in solution deposited tin monosulfide thin films: The role of Pb^{2+} cations, *Mater. Chem. Front.*, 2023, **7**, 3714–3727.
16 E. Segev, U. Argaman, R. E. Abutbul, Y. Golan and G. Makov, A new cubic prototype structure in the IV–VI monochalcogenide system: A DFT Study, *CrystEngComm*, 2017, **19**, 1751–1761.
17 V. E. González-Flores, R. N. Mohan, R. Ballinas-Morales, M. Nair and P. Nair, Thin film solar cells of chemically deposited SnS of cubic and orthorhombic structures, *Thin Solid Films*, 2019, **672**, 62–65.
18 P. Jain and P. Arun, Influence of grain size on the band-gap of annealed SnS thin films, *Thin Solid Films*, 2013, **548**, 241–246.
19 B. Ghosh, R. Bhattacharjee, P. Banerjee and S. Das, Structural and optoelectronic properties of vacuum evaporated SnS thin films annealed in argon ambient, *Appl. Surf. Sci.*, 2011, **257**, 3670–3676.
20 F. De. B. Sánchez, M. T. S. Nair and P. K. Nair, Insights to the production of SnS-cubic thin films by vacuum thermal evaporation for photovoltaics, *Semicond. Sci. Technol.*, 2024, **39**, 015003.
21 M. Calixto-Rodriguez, H. Martinez, A. Sanchez-Juarez, J. Campos-Alvarez, A. Tiburcio-Silver and M. Calixto, Structural, optical, and electrical properties of tin sulfide thin films grown by spray pyrolysis, *Thin Solid Films*, 2009, **517**, 2497–2499.
22 E. Sarica, Investigation of spray pyrolyzed cubic structured Cu doped SnS films, *Phosphorus, Sulfur Silicon Relat. Elem.*, 2021, **196**, 1103–1108.
23 T. Sall, M. Mollar and B. Marí, Substrate influences on the properties of SnS thin films deposited by chemical spray pyrolysis technique for photovoltaic applications, *J. Mater. Sci.*, 2016, **51**, 7607–7613.
24 N. Sato, M. Ichimura, E. Arai and Y. Yamazaki, Characterization of electrical properties and photosensitivity of SnS thin films prepared by the electrochemical deposition method, *Sol. Energy Mater. Sol. Cells*, 2005, **85**, 153–165.
25 Z. Zainal, M. Z. Hussein and A. Ghazali, Cathodic electrodeposition of SnS thin films from aqueous solution, *Sol. Energy Mater. Sol. Cells*, 1996, **40**, 347–357.
26 R. Banai, J. Cordell, G. Lindwall, N. Tanen, S.-L. Shang, J. Nasr, Z.-K. Liu, J. Brownson and M. Horn, Control of phase in tin sulfide thin films produced via RF-sputtering of SnS_2 target with post-deposition annealing, *J. Electron. Mater.*, 2016, **45**, 499–508.
27 V. K. Arepalli and J. Kim, Effect of substrate temperature on the structural and optical properties of radio frequency

sputtered tin sulfide thin films for solar cell application, *Thin Solid Films*, 2018, **666**, 34–39.
28 V. K. Arepalli, Y. Shin and J. Kim, Photovoltaic behavior of the room temperature grown RF-Sputtered SnS thin films, *Opt. Mater.*, 2019, **88**, 594–600.
29 A. A. Voznyi, O. V. Bilousov, B. R. Landeke-Wilsmark, J. Keller, J. Ren, S.-L. Zhang and C. Hägglund, Ultrathin solar cells based on atomic layer deposition of cubic versus orthorhombic tin monosulfide, *ACS Appl. Energy Mater.*, 2021, **4**, 8085–8097.
30 H. Kafashan, M. Azizieh and H. N. Vatan, Ultrasound-assisted electrodeposition of SnS: Effect of ultrasound waves on the physical properties of nanostructured SnS thin films, *J. Alloys Compd.*, 2016, **686**, 962–968.
31 P. O'Brien and J. McAleese, Developing an understanding of the processes controlling the chemical bath deposition of ZnS and CdS, *J. Mater. Chem.*, 1998, **8**, 2309–2314.
32 G. Hodes, *Chemical solution deposition of semiconductor films*, CRC Press, 2002.
33 J. A. Switzer and G. Hodes, Electrodeposition and chemical bath deposition of functional nanomaterials, *MRS Bull.*, 2010, **35**, 743–750.
34 R. Mane and C. Lokhande, Chemical deposition method for metal chalcogenide thin films, *Mater. Chem. Phys.*, 2000, **65**, 1–31.
35 D. Lincot, Solution chemistry and semiconductors: from heterogeneous precipitation to photovoltaic industry, *Actual. Chim.*, 1999, **5**, 23–30.
36 P. Nair, M. Nair, V. Garcıa, O. Arenas, Y. Pena, A. Castillo, I. Ayala, O. Gomezdaza, A. Sanchez and J. Campos, Semiconductor thin films by chemical bath deposition for solar energy related applications, *Sol. Energy Mater. Sol. Cells*, 1998, **52**, 313–344.
37 A. Osherov, V. Ezersky and Y. Golan, The role of solution composition in chemical bath deposition of epitaxial thin films of PbS on GaAs(100), *J. Cryst. Grow.*, 2007, **308**, 334–339.
38 M. Cao, X. Zhang, J. Ren, Y. Sun, Y. Cui, J. Zhang, J. Ling, J. Huang, Y. Shen and L. Wang, Chemical bath deposition of SnS: Cu/ZnS for solar hydrogen production and solar cells, *J. Alloys Compd.*, 2021, **863**, 158727.
39 L. Rodríguez-Guadarrama, J. Escorcia-García, I. Alonso-Lemus and J. Campos-Álvarez, Synthesis of π-SnS thin films through chemical bath deposition: effects of pH, deposition time, and annealing temperature, *J. Mater. Sci.: Mater. Electron.*, 2021, **32**, 7464–7480.
40 E. Guneri, C. Ulutas, F. Kirmizigul, G. Altindemir, F. Gode and C. Gumus, Effect of deposition time on structural, electrical, and optical properties of SnS thin films deposited by chemical bath deposition, *Appl. Surf. Sci.*, 2010, **257**, 1189–1195.
41 A. Tanusevski, Optical and photoelectric properties of SnS thin films prepared by chemical bath deposition, *Semicond. Sci. Technol.*, 2003, **18**, 501–505.
42 J. Jing, M. Cao, C. Wu, J. Huang, J. Lai, Y. Sun, L. Wang and Y. Shen, Chemical bath deposition of SnS nanosheet thin films for FTO/SnS/CdS/Pt photocathode, *J. Alloys Compd.*, 2017, **726**, 720–728.
43 M. S. Mahdi, H. S. Al-Arab, H. S. Al-Salman, K. Ibrahim, N. M. Ahmed, A. Hmood and M. Bououdina, A high performance near-infrared photodetector based on π-SnS phase, *Mater. Lett.*, 2020, **273**, 127910.
44 R. E. Abutbul and Y. Golan, Chemical epitaxy of π-phase cubic tin monosulphide, *CrystEngComm*, 2020, **22**, 6170–6181.
45 M. S. Mahdi, K. Ibrahim, A. Hmood, N. M. Ahmed, F. I. Mustafa and S. A. Azzez, High performance near infrared photodetector based on cubic crystal structure SnS thin film on a glass substrate, *Mater. Lett.*, 2017, **200**, 10–13.
46 V. P. Jethwa, K. Patel, V. Pathak and G. Solanki, Enhanced electrical and optoelectronic performance of SnS crystal by Se doping, *J. Alloys Compd.*, 2021, **883**, 160941.
47 H. Kafashan, Optoelectronic properties of In-doped SnS thin films, *Ceram. Int.*, 2019, **45**, 334–345.
48 F. Jamali-Sheini, M. Cheraghizade and R. Yousefi, Ultrasonic synthesis of In-doped SnS nanoparticles and their physical properties, *Solid State Sci.*, 2018, **79**, 30–37.
49 M. Asghar, H. Ullah, M. W. Iqbal and Y.-H. Shin, Doping dependent optoelectronic, and magnetic properties of monolayer SnS, *Mater. Sci. Semicond. Process.*, 2022, **152**, 107049.
50 I. Ammar, A. Gassoumi and N. Turki-Kamoun, The effect of TSC and nickel doping on SnS thin films, *Silicon*, 2021, **13**, 1933–1938.
51 S. L. Mousavi, F. Jamali-Sheini, M. Sabaeian and R. Yousefi, Correlation of physical features and the photovoltaic performance of P3HT: PCBM solar cells by Cu-doped SnS nanoparticles, *J. Phys. Chem. C*, 2021, **125**, 15841–15852.
52 W. Lei, F. Wang, B. Lu, Z. Ye and X. Pan, Zn-doped SnS with sulfur vacancies for enhanced photocatalytic hydrogen evolution from water, *New J. Chem.*, 2022, **46**, 17791–17800.
53 F. Niknia, F. Jamali-Sheini and R. Yousefi, Examining the effect of Zn dopant on physical properties of nanostructured SnS thin film by using electrodeposition, *J. Appl. Electrochem.*, 2016, **46**, 323–330.
54 S. Sebastian, I. Kulandaisamy, A. Arulanantham, S. Valanarasu, A. Kathalingam, A. J. Jebathew, M. Shkir and M. Karunakaran, Influence of Al doping concentration on the opto-electronic chattels of SnS thin films readied by NSP, *Opt. Quantum Electron.*, 2019, **51**, 1–16.
55 X. Guo, Y. Wang, A. Elbourne, A. Mazumder, C. K. Nguyen, V. Krishnamurthi, J. Yu, P. C. Sherrell, T. Daeneke and S. Walia, Doped 2D SnS materials derived from liquid metal solution for tunable optoelectronic devices, *Nanoscale*, 2022, **14**, 6802–6810.
56 J. Guan, Z. Zhang, M. Dou, J. Ji, Y. Song, J. Liu, Z. Li and F. Wang, Thermoelectric properties of Bi-doped SnS: First-principle study, *J. Phys. Chem. Solids*, 2020, **137**, 109182.
57 K. S. Kumar, C. Manoharan, S. Dhanapandian and A. G. Manohari, Effect of Sb dopant on the structural, optical and electrical properties of SnS thin films by spray pyrolysis technique, *Spectrochim. Acta, Part A*, 2013, **115**, 840–844.

58 V. K. Arepalli, S. J. Kim and J. Kim, Influence of substrate temperature on the growth properties of Ag-doped SnS films deposited by sputtering method, *J. Phys. Chem. Solids*, 2021, **155**, 110099.
59 S. Bano, M. Khan, H. Albalawi, G. U. Islam, M. Siddique, T. Ahmad, H. Alkhaldi, R. Ahson and S. Hussain, Effect of Cd doping on the structural, optical, and photovoltaic properties of SnS films, *J. Mater. Res. Technol.*, 2022, **19**, 1982–1992.
60 M. A. Dar, D. Govindarajan, K. M. Batoo and C. Siva, Supercapacitor and magnetic properties of Fe doped SnS nanoparticles synthesized through solvothermal method, *J. Energy Storage*, 2022, **52**, 105034.
61 A. Javed, Q.-U. Ain and M. Bashir, Controlled growth, structure and optical properties of Fe-doped cubic π-SnS thin films, *J. Alloys Compd.*, 2018, **759**, 14–21.
62 M. Reghima, A. Akkari, C. Guasch, M. Castagné and N. Kamoun-Turki, Synthesis and characterization of Fe-doped SnS thin films by chemical bath deposition technique for solar cells applications, *J. Renewable Sustainable Energy*, 2013, **5**, 063109.
63 F. Niknia, F. Jamali-Sheini and R. Yousefi, Photocurrent properties of undoped and Pb-doped SnS nanostructures grown using electrodeposition method, *J. Electron. Mater.*, 2015, **44**, 4734–4739.
64 S. Sebastian, I. Kulandaisamy, S. Valanarasu, I. Yahia, H.-S. Kim and D. Vikraman, Microstructural and electrical properties evaluation of lead doped tin sulfide thin films, *J. Sol-Gel Sci. Technol.*, 2020, **93**, 52–61.
65 U. Chalapathi, Y. Jayasree and S.-H. Park, Lead-doped cubic tin sulfide thin films for solar cell applications, *Mater. Sci. Semicond. Process.*, 2022, **150**, 106958.
66 N. Mishra, N. Zakay, N. Maman, Y. Golan and G. Makov, Epitaxial growth of π-SnS on PbS substrates, *Cryst. Growth Des.*, 2023, **23**, 2301–2305.
67 B. B. Haidet, E. Hughes and K. Mukherjee, Epitaxial integration and defect structure of layered SnSe films on PbSe/III–V substrates, *Cryst. Growth Des.*, 2022, **22**, 3824–3833.
68 E. T. Hughes, B. B. Haidet, B. Bonef, W. Cai and K. Mukherjee, Pipe-diffusion-enriched dislocations and interfaces in SnSe/PbSe heterostructures, *Phys. Rev. Mater.*, 2021, **5**, 073402.
69 P. Giannozzi, O. Andreussi, T. Brumme, O. Bunau, M. B. Nardelli, M. Calandra, R. Car, C. Cavazzoni, D. Ceresoli, M. Cococcioni, N. Colonna, I. Carnimeo, A. D. Corso, S. de Gironcoli, P. Delugas, R. A. DiStasio Jr, A. Ferretti, A. Floris, G. Fratesi, G. Fugallo, R. Gebauer, U. Gerstmann, F. Giustino, T. Gorni, J. Jia, M. Kawamura, H.-Y. Ko, A. Kokalj, E. Küçükbenli, M. Lazzeri, M. Marsili, N. Marzari, F. Mauri, N. L. Nguyen, H.-V. Nguyen, A. Otero-de-la-Roza, L. Paulatto, S. Poncé, D. Rocca, R. Sabatini, B. Santra, M. Schlipf, A. P. Seitsonen, A. Smogunov, I. Timrov, T. Thonhauser, P. Umari, N. Vast, X. Wu and S. Baroni, QUANTUM ESPRESSO: a modular and open-source software project for quantum simulations of materials, *J. Phys.: Condens. Matter*, 2009, **21**, 395502.
70 K. F. Garrity, J. W. Bennett, K. M. Rabe and D. Vanderbilt, Pseudopotentials for high-throughput DFT calculations, *Comput. Mater. Sci.*, 2014, **81**, 446–452.
71 J. P. Perdew, K. Burke and M. Ernzerhof, Generalized gradient approximation made simple, *Phys. Rev. Lett.*, 1996, **77**, 3865.
72 D. R. Hamann, Optimized norm-conserving Vanderbilt pseudopotentials, *Phys. Rev. B: Condens. Matter Mater. Phys.*, 2013, **88**, 85117.
73 C. Freysoldt, B. Grabowski, T. Hickel, J. Neugebauer, G. Kresse, A. Janotti and C. G. Van de Walle, First-principles calculations for point defects in solids, *Rev. Mod. Phys.*, 2014, **86**, 253.
74 J. Heyd, G. E. Scuseria and M. Ernzerhof, Hybrid functionals based on a screened Coulomb potential, *J. Chem. Phys.*, 2003, **118**, 8207–8215.
75 J. Heyd, G. E. Scuseria and M. Ernzerhof, Erratum: Hybrid functionals based on a screened Coulomb potential (*J. Chem. Phys.* 2003, 118, 8207–8215), *J. Chem. Phys.*, 2006, **124**, 219906.
76 C. G. Van De Walle and J. Neugebauer, First-principles calculations for defects and impurities: Applications to III-nitrides, *J. Appl. Phys.*, 2004, **95**, 3851–3879.
77 E. Segev, U. Argaman and G. Makov, Materials Modelling of π-Phase Monochalcogenides, *Isr. J. Chem.*, 2020, **60**, 876–887.
78 E. Segev, R. E. Abutbul, U. Argaman, Y. Golan and G. Makov, Surface energies and nanocrystal stability in the orthorhombic and π-phases of tin and germanium monochalcogenides, *CrystEngComm*, 2018, **20**, 4237–4248.
79 P. D. Antunez, J. J. Buckley and R. L. Brutchey, Tin and germanium monochalcogenide IV–VI semiconductor nanocrystals for use in solar cells, *Nanoscale*, 2011, **3**, 2399–2411.
80 B. D. Malone, A. Gali and E. Kaxiras, First principles study of point defects in SnS, *Phys. Chem. Chem. Phys.*, 2014, **16**, 26176–26183.
81 E. Segev, U. Argaman, R. E. Abutbul, Y. Golan and G. Makov, A new cubic prototype structure in the IV-VI monochalcogenide system: a DFT study, *CrystEngComm*, 2017, **19**, 1751–1761.
82 R. E. Abutbul, E. Segev, U. Argaman, G. Makov and Y. Golan, π-Phase tin and germanium monochalcogenide semiconductors: an emerging materials system, *Adv. Mater.*, 2018, **30**, 1–8.
83 R. Miranti, R. D. Septianto, T. Kikitsu, D. Hashizume, N. Matsushita, Y. Iwasa and S. Z. Bisri, π-SnS colloidal nanocrystals with size-dependent band gaps, *J. Phys. Chem. C*, 2022, **126**, 5323–5332.
84 Z. Yang, M. Xu, X. Cheng, H. Tong and X. Miao, Manipulation of dangling bonds of interfacial states coupled in GeTe-rich GeTe/Sb_2Te_3 superlattices, *Sci. Rep.*, 2017, **7**, 17353.